BNL-112268-2016-JA

In-Situ Microscopy of Self-Assembly of Branched Nanocrystals in Solution

Eli Sutter[1]

Eli Sutter,[1], Peter Sutter,[2] Alexei V. Tkachenko,[3] Roman Krahne,[4] Joost de Graaf,[5] Milena Arciniegas,[4] Liberato Manna[4]

Submitted to the Journal of Natures Communications

April 2016

Center for Functional Nanomaterials

Brookhaven National Laboratory

U.S. Department of Energy
Office of Basic Energy Sciences

Notice: This manuscript has been authored by employees of Brookhaven Science Associates, LLC under Contract No. DE-SC0012704 with the U.S. Department of Energy. The publisher by accepting the manuscript for publication acknowledges that the United States Government retains a non-exclusive, paid-up, irrevocable, world-wide license to publish or reproduce the published form of this manuscript, or allow others to do so, for United States Government purposes.

DISCLAIMER

This report was prepared as an account of work sponsored by an agency of the United States Government. Neither the United States Government nor any agency thereof, nor any of their employees, nor any of their contractors, subcontractors, or their employees, makes any warranty, express or implied, or assumes any legal liability or responsibility for the accuracy, completeness, or any third party's use or the results of such use of any information, apparatus, product, or process disclosed, or represents that its use would not infringe privately owned rights. Reference herein to any specific commercial product, process, or service by trade name, trademark, manufacturer, or otherwise, does not necessarily constitute or imply its endorsement, recommendation, or favoring by the United States Government or any agency thereof or its contractors or subcontractors. The views and opinions of authors expressed herein do not necessarily state or reflect those of the United States Government or any agency thereof.

In-Situ Microscopy of Self-Assembly of Branched Nanocrystals in Solution

Eli Sutter,[1,*] Peter Sutter,[2] Alexei V. Tkachenko,[3] Roman Krahne,[4] Joost de Graaf,[5] Milena Arciniegas,[4] Liberato Manna[4,*]

[1]*Department of Mechanical and Materials Engineering, University of Nebraska-Lincoln, Lincoln, NE 68588*
[2]*Department of Electrical and Computer Engineering, University of Nebraska-Lincoln, Lincoln, NE 68588*
[3]*Center for Functional Nanomaterials, Brookhaven National Laboratory, Upton, NY 11973, USA*
[4]*Istituto Italiano di Tecnologia (IIT), via Morego 30, IT-16163 Genova, Italy*
[5]*Institute for Computational Physics (ICP), University of Stuttgart, Allmandring 3, 70569 Stuttgart, Germany*

The self-assembly of nanocrystals (NCs) into ordered superstructures has attracted significant interest since the resulting mesoscale objects promise access to a wide range of electronic,[1] photonic,[2] plasmonic,[3,4] magnetic,[5] and catalytic[6] functionalities that may be tuned by proper choice of the NC building blocks or superstructure characteristics and may even be reconfigurable in real time.[7] NC self-assembly can be controlled via the interplay of van der Waals forces with entropic, steric, and dipolar interactions,[8,9] by attaching molecular linkers such as coordinated ligands or DNA,[10] or by using shaped NCs.[11] Liquid environments are key to self-assembly since they allow suspended NCs to diffuse and interact freely, but they also complicate experiments. Usually, only the final assemblies are characterized ex-situ; in-situ measurements have largely been limited to reciprocal space techniques,[10,12] which yield limited information at the single-particle level that could shed light on the assembly process or the underlying forces. Liquid-cell electron microscopy (LCEM) has recently been developed into a tool capable of imaging processes in liquids in-situ with nanometer spatial resolution.[13-15] Here we use this in-situ and real-time imaging capability of LCEM to elucidate the nucleation and growth mechanism of linear chains of octapod-shaped NCs, and to assess key aspects of the ordered chains (length, monomer equilibrium spacing) in their native solution environment. Statistical mechanics modeling based on these observations and using the measured chain length distribution clarifies the relative importance of van der Waals and entropic forces in the assembly process, and provides direct access to the strength of the interparticle interaction. Our results suggest that monomer-resolved in-situ imaging combined with modeling can provide unprecedented quantitative insight into the microscopic processes and interactions that govern self-assembly in solution.

[*]Correspondence and requests for materials should be addressed to ES (e-mail: esutter@unl.edu) and LM (e-mail: liberato.manna@iit.it).

In-situ electron microscopy in liquids has demonstrated great versatility in imaging phenomena such as colloidal synthesis (nanoparticles,[13] nanorods,[16] core-shell structures[17,18]), electrochemistry (galvanic replacement reactions,[19] electrodeposition,[14] fuel cells[20]), as well as biological systems.[21] The in-situ observation of self-assembly processes has been demonstrated for NCs with simple polyhedral shapes.[22] We extend LCEM to visualizing the self-assembly of CdSe/CdS octapods (Fig. 1) in real space with nanometer resolution. Octapods, archetypal branched nanocrystals with a complex but still highly symmetric shape of interest as functional components in nanodevices,[23-25] have been found to self-assemble into a variety of superstructures: interlocked one-dimensional (1D) chains in bulk liquid, 2D square lattices on rigid substrates,[26] or micron-sized 3D structures of aligned 1D chains.[12] Strongly anisotropic interactions between branched nanocrystals are thought to be key to their rich set of accessible superstructures.

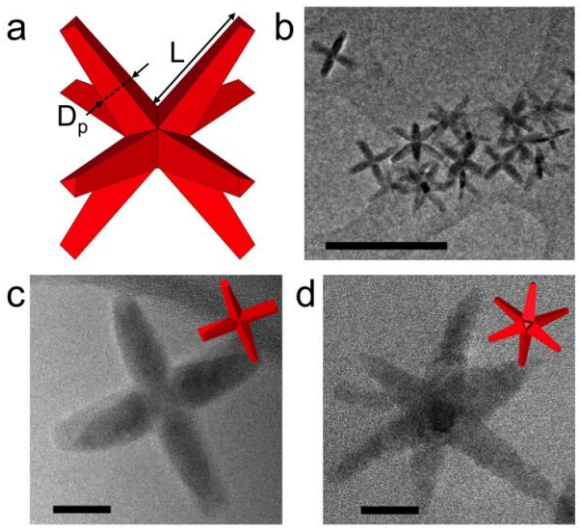

Figure 1. CdSe/CdS octapods and liquid cell. a. Schematic geometry of a single octapod-shaped CdSe/CdS nanocrystal. **b.** TEM image of a group of octapod-shaped CdSe/CdS nanocrystals drop-cast onto amorphous carbon film. Scale bar: 200 nm. **c, d.** High-magnification TEM images of octapods with different orientations, as illustrated. Scale bars: 20 nm.

In-situ microscopy was performed by scanning TEM (STEM) using solutions of CdSe/CdS octapods (pod length L ~ (47 ± 3) nm, pod aspect ratio L/D_p ~ 4.2; Fig. 1) in toluene with a nominal particle concentration of 10^{-8} M, prepared according to reported methods.[12] The solution was loaded in the liquid cell and observed within a viewing area in which it was held between two electron transparent SiN_x membranes (see Methods for details). Immediately after starting the observations, there was a higher concentration of octapods near the corners of the cell and along the edges of the window, whereas the center of the cell remained less populated.

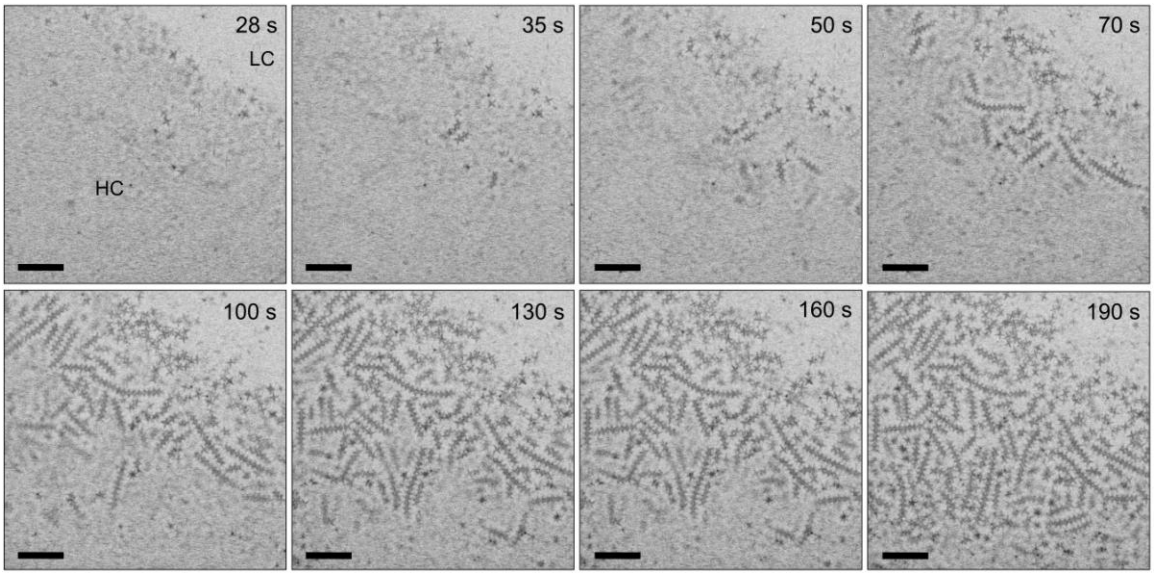

Figure 2. In-situ liquid-cell STEM of the assembly of octapods into linear chains: Selected inverted dark-field STEM images from movie M1 showing the formation of ordered chains of octapods in toluene. Scale bars: 500 nm. The images show the evolution of the system, starting from single octapods dispersed in the entire liquid volume (for t < 30 s, "HC": high concentration of octapods; "LC": low concentration) to interlocked chain-like structures that aggregate near the top membrane of the liquid cell.

Fig. 2 shows a representative sequence of liquid-cell STEM images of octapods in toluene (extracted from movie M1) that follows the time evolution near the boundary between high and low concentration. Initially (observation time t < 30 s) the solution

within these areas appears homogeneous, with diffuse contrast and streaking suggesting dispersed individual octapods (high atomic number, Z) and possibly chains submerged in the bulk solvent. As the self-assembly progresses, octapods and linear chains are clearly observed ($t \geq 35$ s). Chains of interlocked octapods form exclusively in the region with higher concentration near the edges and corners of the viewing window (Fig. S7). The first clear contrast is due to two short chain segments, each containing three interlocked octapods ($t = 35$ s). In the next ~20 s, additional short chains become visible and the first longer chains appear; surrounding diffuse contrast indicates continuing rapid motion in the solvent. During the further evolution, the existing chains grow longer so that the field-of-view (FOV) becomes progressively crowded with interlocked octapod chains of different length. An overall downward directionality might be interpreted as a sign of progressive drying of the solvent and concomitant increase of the octapod density in the remaining solution, such as in evaporative self-assembly processes[27,28] reported previously. Further examination shows, however, that the formation of octapod chains occurs in a 3D solution environment of constant thickness, and is not significantly influenced by evaporation of the toluene solvent (see Supplementary Material).

Analysis of real-time image sequences allows us to develop a detailed picture of the self-assembly of 1D octapod chains in solution. Important elements, such as image contrast, predominant octapod orientations, and a limited 3D imaging capability in STEM are discussed in the Supplementary Material (Fig. S2). Fig. 2 and additional data (movies M2-M6; extracted images in Fig. 3, Figs. S10-S14) document the assembly mechanism. The process is initiated by the emergence of short segments of tightly interlocked octapod chains. The majority of chains are built from interlocked units, similar to those analyzed

ex-situ in vitrified solvent,[12] but observations of pairs or larger numbers of monomers interacting tip-to-tip and diffusing as a non-interlocked cluster (movies M2, M3) suggest a richer set of interactions between monomers than the pod-to-pod van der Waals forces invoked so far.

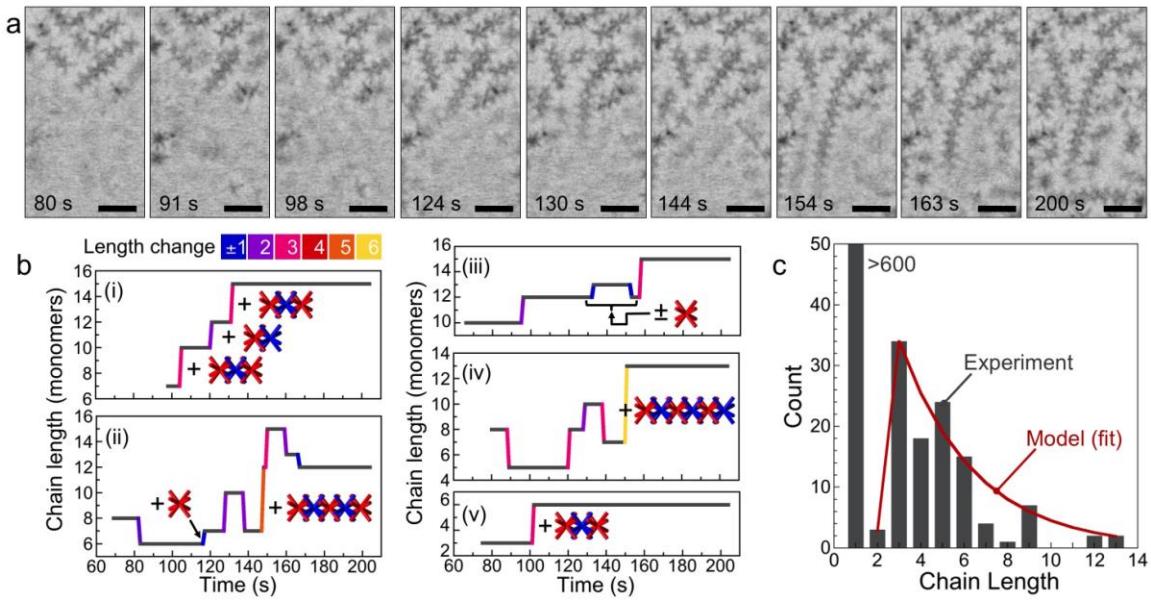

Figure 3. Imaging octapod chains and tracking their growth with monomer resolution; modeling of the assembly process. a. Representative time-lapse series of inverted dark-field STEM images showing the growth of a long chain of interlocked octapods. Scale bar: 200 nm. **b.** Representative traces of the length as a function of time of interlocked octapod chains, showing changes in length occurring only in exceptional cases by addition or removal of monomers, but instead mostly via incorporation and detachment of longer oligomers. Length changes are color-coded as shown above panel (i). Longer horizontal lines imply that the length of the chain stays unchanged for extended time periods. **c.** Length distribution of interlocked octapod chains, determined by ex-situ STEM after opening the liquid cell (gray bars; total sample size: 752 objects, of which 642 were individual octapods). Note the absence of interlocked dimers. Red line: best fit of the length distribution within the statistical mechanics model described in the text.

Short interlocked octapod chains typically emerge from the bulk solution, which indicates that they are formed there. Observations of the fluid with focal plane near the top SiN_x membrane show the attachment and detachment of such short chain segments as the predominant process of forming long 1D chains (Fig. 2). Chain growth is clearly a

dynamic process, subject to fluctuations that add and remove segments of varying length (Fig. 3 a, b). The smallest interlocked oligomer unit observed in our experiments is the trimer, i.e., consists of three octapods. A survey of a large number of chains ex-situ after opening the liquid cell (Fig. 3 c) and in-situ at different stages of the assembly (Fig. 4) shows only isolated instances of interlocked dimers, whereas trimers and longer chains are much more abundant. The addition of a trimers and longer oligomers is also the predominant elementary step in chain growth (Fig. 3 b), while monomer incorporation is quite rare and is often followed by detachment of the same unit, suggesting incomplete locking (e.g., Fig. 3 b, (iii)). Two-octapod increments are occasionally seen (e.g., Fig. 3 b, (i), (iii), (iv)) but the absence of stable dimers in the solution suggests that these instances may actually represent a sequential addition of monomers or of non-interlocked dimers.

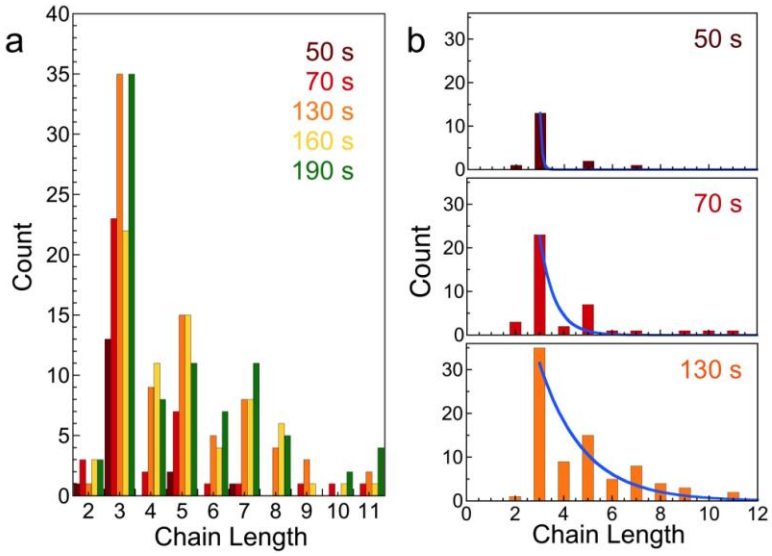

Figure 4. Time evolution of octapod chain length distribution. a. Length distribution of interlocked octapod chains, determined by in-situ STEM at different times during the self-assembly. **b.** Chain length distributions at the early stages of self-assembly. The blue lines are exponential fits for chain lengths ≥ 3.

The observed solution-phase self-assembly deviates from a classic nucleation and growth scenario, which presumes the formation of a stable nucleus followed by attachment of monomer units.[29] While there appears to be a stable nucleus, the trimer, the further growth in most cases does not involve the incorporation of individual octapods even though monomers are abundant and show extensive Brownian motion. Instead, the stable nucleus grows primarily by attachment of other supercritical units, all of which are mobile in the solution. Attachment is facilitated by a considerable bending flexibility of the chains, which, for instance, allows long chains near the membrane to reach into the bulk liquid to capture a diffusing segment (Fig. 3 a; Fig. S10; movie M4).

We constructed a model to probe the physical origin of the striking suppression of dimers and the prevalence of trimers as the shortest chain of interlocked octapods in solution. Using the measured chain length distribution and other characteristics identified uniquely by in-situ microscopy, the model provides insight into the interactions underlying the self-assembly process. In equilibrium, the probability of finding a chain of length n can be determined from the grand canonical distribution function:

$$C_n \propto \int d\Gamma \, e^{-\beta[H-\mu n]}$$

Here the chemical potential of otapods is determnined by the concentration of monomers C_1, as $\mu = kT \ln C_1$; H is the interaction Hamiltonian of the system, $\beta = 1/kT$, and $d\Gamma$ represents an integration over internal degrees of freedom on the chain, i.e. positions and orientations of $n-1$ octapods. If we neglect physical binding between the octapods (i.e. assume $H = 0$, but exclude their mutual overlap), the confinement of a single octapod within a cage made by two of its neighbors, can be represented as a factor v. This factor has a meaning of effective localization volume and it accounts for the loss of translational

and orientational entropies of the confined octapod. If Δ is a typical range of its translational fluctuations, the corresponding amplitude of the angular degrees of freedom is Δ/R, where R is a characteristic radius of the octapod. Therefore an integration over three translational and three orientational degrees of freedom gives an effective localization volume $v \sim \Delta^6/R^3$.

We now can take into account mutual binding of the octapods. In our model, two octapods in contact create a reversible bond, each having the same characteristic binding energy $-\epsilon$ and the localization range δ (set by the length of the ligands and estimated to be $\sim 2.5\ nm$). We represent these bonds as a collection of two-state systems that can be in a "bound" or an "unbound" state independently of each other. This leads to the following distribution function:

$$C_n \sim (C_1 v)^{n-1} \left(1 + \frac{\delta}{\Delta} e^{\epsilon/kT}\right)^{Z_n}$$

An alternative, and more detailed derivation of this result is presented as a part of Supplementary Information. In this equation, Z_n is the total number of contacts between the octapods that can be independently formed within the chain. This parameter is of crucial importance for understanding the observed chain statistics, in particular the substantial suppression of dimers compared to larger (longer) clusters. We assume the maximum number of contacts that can be made between nearest neighbors to be 4. This implies that a tighter interlocking of two octapods with 8 mutual contacts is not sterically allowed, presumably because of the geometry of their octahedral cores. This is consistent with the experimental observations (see below). In addition to the interactions with its nearest neighbors, it is assumed that fluctuations in the chain allow an octapod to create

up to 4 contacts with any of its next-nearest neighbors. This consideration sets the upper bound to the number of contacts in a chain: $Z_n \leq 4(n-1) + 4(n-2) = 8n - 12$. However, this is not the only limitation. Each octapod has 6 degrees of freedom: 3 translational, and 3 rotational. This means that for trimers (n = 3) the number of possible contacts (12) is exactly equal to the number of internal degrees of freedom of the chain, $6(n-1)$. For dimers (n = 2), the number of contacts is less than the number of degrees of freedom (4 and 6, respectively), while for chains longer than n = 3, the situation is opposite. The maximally connected structure with $Z_n = 8n - 12$ would be over-constrained, and can only exist if the shapes are identical and symmetric to within a very high precision. Any imperfection would lead to a loss of some of the contacts. We therefore postulate that the number of internal degrees of freedom sets another bound on the value of Z_n, i.e.,

$$Z_n = \min\big(8n - 12\,, 6(n-1)\big)$$

This model can successfully describe the observed chain statistics, including the suppression of dimers. In fact, its major features predicted by the model are very robust with respect to the choice of the model parameters. For $n \geq 2$, $Z_n = 6(n-1)$ and therefore the overall distribution function is proportional exponential: $C_n \propto p^{n-1}$ where $p = (C_1 v)\left(1 + \delta e^{\frac{\epsilon}{kT}}/\Delta\right)^6$. For $n = 2$, the number of contacts is 4, which is smaller than $6(n-1) = 6$. This leads to a relative suppression of dimers by a factor $(C_1 v)^{1/3}$.

As far as the specific parameters are concerned, the characteristic radius of the octapod R is taken to be $\sim 30\ nm$, i.e., half of a pod length; the value of $\Delta \approx 15\ nm$ was estimated as the difference between the apparent inter-particle distance in the chain ($50\ nm$) and its

minimal value allowed geometrically ($35\ nm$). The estimated average concentration of free octapods in the area in which self-assembly takes place is $C_1 \sim 10^{-6}\ M \sim 10^{-6}\ nm^{-3}$, so that $C_1 v \sim C_1 \Delta^6 / R^3$ is of the order of 10^{-3}. Once the geometrical parameters are fixed, the only fitting parameter of the model is the energy per contact, ϵ.

The value of the energy ϵ that gives the best fit to the experimental data is $2.7\ kT$ (Fig. 3 c). This value is approximately twice as large as the energy expected for pure van der Waals interaction between two crossed pods.[12] The difference may be due to effects of interdigitation of the ligands. The robustness of our model can be illustrated by the fact that changing $C_1 v$ by factor of 2 leads to a correction to the binding strength ϵ of $0.1\ kT$, and to the relative change of dimer fraction of only 25%.

In addition to this statistical mechanical model, we have performed MD simulations of a small system of octapods that also support the observation that a pure van der Waals interaction is not sufficient to induce assembly (see Supplementary Information). The addition of a short-range attraction does lead to chain formation.

In our model the assembly is driven not only by the energy gained due to binding. The fact that each contact fluctuates between "bound" and "unbound" states results in an additional entropic free energy contribution $-6kT \ln\left(1 + \frac{\Delta}{\delta} e^{-\epsilon/kT}\right) \approx -2\ kT$ per particle that stabilizes the chain. One final piece of evidence that points in the direction of the proposed mechanism stems from measurements of the octapod spacing in chains, a characteristic that was determined by in-situ imaging to avoid uncertainties due to capillary forces that may affect ex-situ measurements of the lattice constant of stabilized (dried or vitrified) assemblies. The observed distance between the next-nearest neighbor

octapods in the chains ($\approx 100\ nm$, observed in situ (Fig. 5 a)) is in fact greater than the one needed for a physical contact between four tips of the two octapods ($\approx 85\ nm$, close to the value found ex situ for chains in vacuum (Fig. 5 b) or vitrified solvent[12]). This distance is however sufficient to make up to 2 contacts simultaneously upon some rotation. In this way, the system can achieve the required value of Z_n (6 per particle) without paying an excessive entropic penalty for the extra confinement. The loose stacking in solution also rationalizes characteristics important to chain growth, such as the facile addition and removal of chain segments and the bending of chains in tight radii, involved in capturing chain segments at the later growth stages.

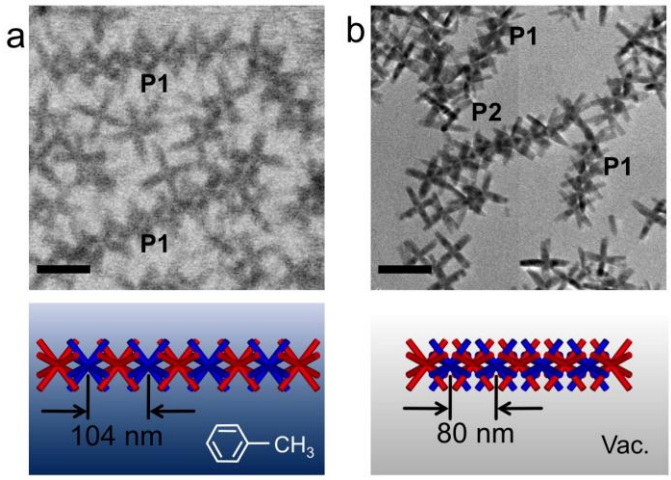

Figure 5. Comparison of the spacing in interlocked octapod chains in toluene and in vacuum after opening the liquid cell. a. Octapod chains in toluene, imaged by liquid-cell STEM. Two longer chains are imaged in projection **P1 (**see Supplementary Material). Scale bar: 100 nm. **b.** Octapod chains in projections **P1** and **P2** imaged by TEM in vacuum after opening the liquid cell, shown at the same scale as a. Scale bar: 100 nm. Note the substantially larger nearest-neighbor spacing observed in toluene solution (52 ± 2 nm) compared to the dried assemblies (40 ± 2 nm), which suggests that capillary forces acting on the particles upon drying of the solvent (and during freezing for cryo-TEM in vitrified toluene)[12] cause a significant tightening of the chains.

By observing the self-assembly of octapod-shaped, branched nanocrystals with monomer resolution in toluene solution, our experiments have pointed out a novel avenue for studying key aspects of self-assembly, such as the mechanism of formation and growth of ordered nanocrystal arrays and the interparticle spacing in solution. Taking into account the characteristics obtained from in-situ microscopy, a statistical model could be built that established the relative importance of Van der Waals and entropic forces and determined the strength of the particle-particle interaction. These findings open up new perspectives for the use of in-situ microscopy to understand and harness nanoparticle self-assembly. A similar approach can be applied to other systems, such as particles that arrange in 2D or 3D assemblies, binary or more complex mixtures of nanocrystals, or the folding and assembly of suitably tagged proteins. Once cells are developed that allow for controlled mixing of different liquids, external stimuli (e.g., changes in PH, addition of a co-solvent, etc.) may be used to actively change the assembly process while observing the outcome in real time.

Materials and Methods

CdSe/CdS octapod-shaped nanocrystals were synthesized following our procedure based on the growth of CdS pods on cuboctahedral CdSe seeds that are prepared after a cation exchange process from $Cu_{2-x}Se$ nanocrystals. Briefly, a reaction flask was loaded with 120 mg of CdO and various surfactants (6 g of trioctylphosphine oxide, 160 mg of hexylphosphonic acid and 580 mg of octadecylphosphonic acid). The flask was kept under vacuum at 150°C for 120 min. The temperature was increased to 350°C and 1.6 g of trioctylphosphine (TOP) was injected. After the recovery of the temperature, an aliquot

of previously prepared $Cu_{2-x}Se$ nanocrystals with a concentration of 0.3×10^{-9} M was quickly injected in the flask after the addition of 16:0.5 mg S/TOP solution. The reaction was run for 10 min and cooled down to room temperature. After several washing steps with an antisolvent, the final product was dispersed in 5 ml of toluene or chloroform.

The liquid cell experiments were carried out in a dedicated specimen holder (Hummingbird Scientific) using microfabricated liquid cells, consisting of two 30 nm thick SiN_x membrane windows with 50 µm x 50 µm window area supported by Si frames. The spacing between the windows was controlled using 200 nm and 300 nm polystyrene beads or 100 nm and 200 nm SiO_2 spacers. (S)TEM imaging was performed in a FEI Titan 80-300 environmental Cs image corrected microscope operated at 300 kV. Low-loss electron energy loss spectra (EELS) were acquired using a Gatan Enfina spectrometer with an entrance aperture semiangle of 5 mrad. The weighted average of the ratio of the thickness and the inelastic mean free path for the toluene and the 2 SiN membranes (each 30 nm thick) was determined from the low-loss EELS, and the toluene thickness was calculated from it according to reference [30]. Typically ~1 µL of the octapod-containing solution with an initial concentration of particles of 10^{-8} M were introduced in the liquid cell. The holder was inserted in the microscope immediately after the loading of the liquid cell. The time delay between loading of the solution and initiating the observations was ~10 - 20 minutes. STEM imaging was performed with ~ 2Å probe size and ~ 0.2 - 0.3 nA beam current, measured in vacuum prior to introduction of the liquid cell. Time-lapse series of STEM images were acquired at several positions along the cell window, and at all positions the assembly of octapods was observed in real time. The results of the observations at two different areas are shown in movies M1 and

M8. For movies M1-M7 time-lapse STEM images of the assembly of the octapods were recorded with frame interval of 1 s and 3.96 μs dwell time/pixel. The conditions for the acquisition of STEM images were: electron dose rate of 1.35 $e^{-}Å^{-2}s^{-1}$, electron dose per image of 1.35 $e^{-}Å^{-2}$, total electron dose for the movie (204 frames) of 275.4 $e^{-}Å^{-2}$. Movies M1-M7 are played at 20 frames/s. The original STEM images are shown in Fig. S1. The STEM images in which the octapods appear dark on a light background have been inverted (in the program ImageJ) to facilitate visual perception and analysis. Movie M8 is a series of time-lapse images recorded at a frame interval of 9 seconds.

Acknowledgements

This research has been carried out in part at the Center for Functional Nanomaterials, Brookhaven National Laboratory, which is supported by the U.S. Department of Energy, Office of Basic Energy Sciences, under Contract No. DE-SC0012704. LM and MA acknowledge financial support from the European Union through the FP7 starting ERC grant NANO-ARCH (contract number 240111). We thank K. Jungjohann for the measurement of EELS spectra and E. Krings for analyzing the chain length distributions. JdG acknowledges financial support from the NWO Rubicon grant (#680501210) and Prof. A. Arnold and Dr. O. Hickey for useful discussions.

Author Contributions

ES conceived the study, performed in-situ microscopy experiments, analyzed the data, and co-wrote the paper. PS analyzed the data and co-wrote the paper. RK conceived the experiment and contributed to data analysis, discussion, interpretation of data and paper writing. JdG performed numerical simulations, contributed to the discussion of the results

and paper writing. AT conceived the model explaining the octapod chain-length distribution. MA contributed to data analysis, discussion, interpretation of data and paper writing. LM contributed to data analysis, discussion, interpretation of data and paper writing. All authors commented on the manuscript.

References

1. Choi, J.-H. *et al.* Bandlike Transport in Strongly Coupled and Doped Quantum Dot Solids: A Route to High-Performance Thin-Film Electronics. *Nano Letters* **12**, 2631-2638 (2012).
2. Sun, L. *et al.* Bright infrared quantum-dot light-emitting diodes through inter-dot spacing control. *Nat Nano* **7**, 369-373 (2012).
3. Ye, X., Chen, J., Diroll, B. T. & Murray, C. B. Tunable Plasmonic Coupling in Self-Assembled Binary Nanocrystal Superlattices Studied by Correlated Optical Microspectrophotometry and Electron Microscopy. *Nano Letters* **13**, 1291-1297 (2013).
4. Tao, A., Sinsermsuksakul, P. & Yang, P. Tunable plasmonic lattices of silver nanocrystals. *Nat Nano* **2**, 435-440 (2007).
5. Chen, J. *et al.* Collective Dipolar Interactions in Self-Assembled Magnetic Binary Nanocrystal Superlattice Membranes. *Nano Letters* **10**, 5103-5108 (2010).
6. Yamada, Y. *et al.* Nanocrystal bilayer for tandem catalysis. *Nat Chem* **3**, 372-376 (2011).
7. Kim, Y., Shah, A. A. & Solomon, M. J. Spatially and temporally reconfigurable assembly of colloidal crystals. *Nat Commun* **5** (2014).
8. Collier, C. P., Vossmeyer, T. & Heath, J. R. Nanocrystal Superlattices *Annual Review of Physical Chemistry* **49**, 371-404 (1998).
9. Shevchenko, E. V., Talapin, D. V., Kotov, N. A., O'Brien, S. & Murray, C. B. Structural diversity in binary nanoparticle superlattices. *Nature* **439**, 55-59 (2006).
10. Nykypanchuk, D., Maye, M. M., van der Lelie, D. & Gang, O. DNA-guided crystallization of colloidal nanoparticles. *Nature* **451**, 549-552 (2008).
11. Maye, M. M., Kumara, M. T., Nykypanchuk, D., Sherman, W. B. & Gang, O. Switching binary states of nanoparticle superlattices and dimer clusters by DNA strands. *Nat Nano* **5**, 116-120 (2010).
12. Miszta, K. *et al.* Hierarchical self-assembly of suspended branched colloidal nanocrystals into superlattice structures. *Nature Materials* **10**, 872-876 (2011).
13. Zheng, H. M. *et al.* Observation of Single Colloidal Platinum Nanocrystal Growth Trajectories. *Science* **324**, 1309-1312 (2009).
14. Williamson, M. J., Tromp, R. M., Vereecken, P. M., Hull, R. & Ross, F. M. Dynamic microscopy of nanoscale cluster growth at the solid-liquid interface. *Nature Materials* **2**, 532-536 (2003).

15. Yuk, J. M. *et al.* High-Resolution EM of Colloidal Nanocrystal Growth Using Graphene Liquid Cells. *Science* **336**, 61-64 (2012).
16. Liao, H. G., Cui, L. K., Whitelam, S. & Zheng, H. M. Real-Time Imaging of Pt_3Fe Nanorod Growth in Solution. *Science* **336**, 1011-1014 (2012).
17. Jungjohann, K. L., Bliznakov, S., Sutter, P. W., Stach, E. A. & Sutter, E. A. In Situ Liquid Cell Electron Microscopy of the Solution Growth of Au–Pd Core–Shell Nanostructures. *Nano Letters* **13**, 2964-2970 (2013).
18. Sutter, E. A. & Sutter, P. W. Determination of Redox Reaction Rates and Orders by In Situ Liquid Cell Electron Microscopy of Pd and Au Solution Growth. *Journal of the American Chemical Society* **136**, 16865–16870 (2014).
19. Sutter, E. *et al.* In-situ Liquid Cell Electron Microscopy of Ag-Pd Galvanic Replacement Reactions on Ag Nanoparticles. *Nature Communications* **5**, 4946-4954 (2014).
20. Gu, M. *et al.* Demonstration of an Electrochemical Liquid Cell for Operando Transmission Electron Microscopy Observation of the Lithiation/Delithiation Behavior of Si Nanowire Battery Anodes. *Nano Letters* **13**, 6106-6112 (2013).
21. de Jonge, N., Peckys, D. B., Kremers, G. J. & Piston, D. W. Electron microscopy of whole cells in liquid with nanometer resolution. *Proceedings of the National Academy of Sciences of the United States of America* **106**, 2159-2164 (2009).
22. Park, J. *et al.* Direct Observation of Nanoparticle Superlattice Formation by Using Liquid Cell Transmission Electron Microscopy. *ACS Nano* **6**, 2078-2085 (2012).
23. Li, H., Kanaras, A. G. & Manna, L. Colloidal Branched Semiconductor Nanocrystals: State of the Art and Perspectives. *Accounts of Chemical Research* **46**, 1387-1396 (2013).
24. Glotzer, S. C. & Solomon, M. J. Anisotropy of building blocks and their assembly into complex structures. *Nat Mater* **6**, 557-562 (2007).
25. Conca, E. *et al.* Charge separation in Pt-decorated CdSe@CdS octapod nanocrystals. *Nanoscale* **6**, 2238-2243 (2014).
26. Qi, W. *et al.* Ordered Two-Dimensional Superstructures of Colloidal Octapod-Shaped Nanocrystals on Flat Substrates. *Nano Letters* **12**, 5299-5303 (2012).
27. Brinker, C. J., Lu, Y., Sellinger, A. & Fan, H. Evaporation-Induced Self-Assembly: Nanostructures Made Easy. *Advanced Materials* **11**, 579-585 (1999).
28. Rabani, E., Reichman, D. R., Geissler, P. L. & Brus, L. E. Drying-mediated self-assembly of nanoparticles. *Nature* **426**, 271-274 (2003).
29. De Yoreo, J. J. & Vekilov, P. in *Biomineralization* (eds Dove P.M., De Yoreo J.J., & Weiner S.) 57-93 (Mineral Soc. Am., 2003).
30. Egerton, R. F. *Electron energy loss spectroscopy in the electron microscope*. (Plenum Press, (1996)).